Journal Pre-proof

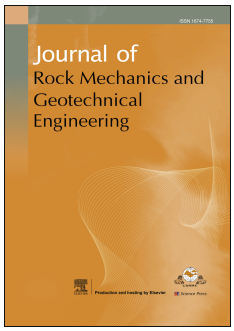

Effect of lateral stress on frictional properties of a fracture in sandstone

Zhechao Wang, Jinmeng Zhao, Derek Elsworth, Xia-Ting Feng, Pengyu Wang

PII: S1674-7755(24)00244-0

DOI: https://doi.org/10.1016/j.jrmge.2024.04.010

Reference: JRMGE 1577

To appear in: *Journal of Rock Mechanics and Geotechnical Engineering*

Received Date: 2 February 2024

Revised Date: 18 March 2024

Accepted Date: 14 April 2024

Please cite this article as: Wang Z, Zhao J, Elsworth D, Feng X-T, Wang P, Effect of lateral stress on frictional properties of a fracture in sandstone, *Journal of Rock Mechanics and Geotechnical Engineering*, https://doi.org/10.1016/j.jrmge.2024.04.010.

Full Length Article

Effect of lateral stress on frictional properties of a fracture in sandstone

Zhechao Wang[a, b, *], Jinmeng Zhao[a, b], Derek Elsworth[c], Xia-Ting Feng[a, b], Pengyu Wang[a, b]

[a] Institute of Deep Engineering and Intelligent Technology, Northeastern University, Shenyang, 110819, China

[b] Liaoning Provincial Research Center on Underground Storage Engineering, Shenyang, 110819, China

[c] Energy and Mineral Engineering, EMS Energy Institute and G3 Center, Pennsylvania State University, University Park, 16802, USA

*Corresponding author. E-mail address: wangzhechao@mail.neu.edu.cn (Z. Wang)

Abstract: The injection of large volumes of natural gas into geological formations, as is required for underground gas storage, leads to alterations in the effective stress exerted on adjacent faults. This increases the potential for their reactivation and subsequent earthquake triggering. Most measurements of the frictional properties of rock fractures have been conducted under normal and shear stresses. However, faults in gas storage facilities exist within a true three-dimensional (3D) stress state. A double-direct shear experiment on rock fractures under both lateral and normal stresses was conducted using a true triaxial loading system. It was observed that the friction coefficient increases with increasing lateral stress, but decreases with increasing normal stress. The impact of lateral and normal stresses on the response is primarily mediated through their influence on the initial friction coefficient. This allows for an empirical modification of the rate-state friction model that considers the influence of lateral and normal stresses. The impact of lateral and normal stresses on observed friction coefficients is related to the propensity for the production of wear products on the fracture surfaces. Lateral stresses enhance the shear strength of rock (e.g. Mogi criterion). This reduces asperity breakage and the generation of wear products, and consequently augments the friction coefficient of the surface. Conversely, increased normal stresses inhibit dilatancy on the fracture surface, increasing the breakage of asperities and the concomitant production of wear products that promote rolling deformation. This ultimately reduces the friction coefficient.

Keywords: Sandstone fracture; Friction coefficient; Lateral stress; Normal stress; Shear rate; Rate-state friction model

1. Introduction

The transformation to a low-carbon economy has become an inevitable choice for strategic development, and natural gas can play a distinctive role in this regard. Underground gas storage is an effective method to guarantee peak supply, which plays an important role in ensuring the safe and stable supply of natural gas. However, the injection of large volumes of natural gas into subsurface formations will result in elevated pressures and alternations to the effective stress and strength of faults in the vicinity of the storage facility (Ellsworth, 2013; He et al., 2021). The injected gas induces stress changes in any potential fault. The reactivation of a fault can induce frictional slip (Leeman et al., 2016; Leeman et al., 2018), thereby reducing the security of the gas storage. Furthermore, fault slip may also serve as a significant contributing factor in seismic activity (Brace and Byerlee, 1966). Therefore, laboratory-based experiments on rock fracture friction are of significant value in enhancing our understanding of both gas storage stability and earthquake mechanisms (Ben-David et al., 2010; Zhang et al., 2023; Zhong et al., 2023).

In the context of frictional sliding, variables such as normal stress (Li et al., 1987; Cui et al., 2005; Mehrishal et al., 2016) and shear velocity (Marone, 1998; Miao et al., 2012; Dong et al., 2018) exert a significant influence on the frictional characteristics of the fracture surfaces. In terms of the influence of normal stress, Han and Kang (2013) found that under low normal stress conditions, the friction coefficient of a granite surface decreases as the normal stress increases, while at high normal stresses, it increases. Liu et al. (2023) observed a decrease in the friction coefficient of fracture in tight sedimentary rocks with increasing normal stress, as evidenced by both experimental and numerical models. Regarding the influence of shear velocity, shearing of granite under a normal stress of 50 MPa and a shear velocity range of 0.001–3 mm/s has demonstrated velocity weakening at shear velocities below 10 μm/s, with a negative correlation between the friction coefficient and increased shear velocity (Blanpied et al., 1987). Conversely, shear velocities exceeding 32 μm/s exhibited velocity strengthening, with the friction coefficient increasing with higher shear velocities. At normal stresses of 5–150 MPa and sliding velocities of 10^{-4}–10^{3} μm/s, velocity weakening is apparent at velocities below 10 μm/s, regardless of the normal stresses (Kilgore et al., 1993). At high normal stresses, velocity weakening was observed beyond 10 μm/s, while velocity strengthening was observed at low normal stress (5 MPa). Moreover, some literature has examined the influence of

temperature (Liu and He, 2023; Noda, 2023), inhomogeneous friction interface (Wang et al., 2023a), and fault gouge (Zhong et al., 2024) on the frictional properties of rock fractures. It is notable that the influence of lateral stress is absent in the aforementioned studies.

Laboratory tests on frictional properties include direct shear tests (Feng et al., 2021; Tatnell et al., 2021), triaxial tests (Marone et al., 1990; Wang et al., 2023b), and double-direct shear tests (Collettini et al., 2014). Direct shear tests load a single fracture, but may present an intricate internal stress state. In triaxial friction tests, the shear displacement of the rock fracture cannot be measured directly. For double-direct shear tests, the specimens are loaded by moving the center block, which keeps the contact area between the platens and the specimen the same even after significant shear displacements. This eliminates any additional torque generation and enables a robust evaluation of rock friction.

Currently, laboratory tests on rock fracture friction are primarily conducted in single and double-direct shear modes without lateral pressure. However, there is a paucity of experimental or theoretical studies investigating the influence of lateral stress on the frictional properties of rock fractures. It is crucial to comprehend the frictional characteristics of rock fractures under both normal and lateral stresses as underground gas storage facilities are subjected to a true three-dimensional (3D) stress state. This study conducts double-direct shear tests on rock fractures subjected to lateral stress using a triaxial loading system. The objective is to investigate the influence of lateral stress, normal stress, shear velocity, and shear displacement on the friction coefficient. Based on these experimental results, we propose a modified friction constitutive model that incorporates the influence of both lateral and normal stresses. Furthermore, we elucidate potential mechanisms for how lateral and normal stresses affect the friction coefficient based on our experimental observations.

2. Methodology

2.1. Specimen Preparation

The rock specimens utilized in the experiment were red sandstone. The rocks were cut into prisms, with a controlled surface roughness (*Ra*) of the cutting surfaces at 1.6 μm. For the double-direct shear specimens, two blocks of 50 mm × 20 mm × 50 mm (length × width × height) and one center block of 70 mm × 20 mm × 50 mm were prepared, as shown in Fig. 1. The rock blocks were carefully machined to ensure a uniform distribution of lateral stress across the specimen, guaranteeing that all specimen groups were of compatible dimensions.

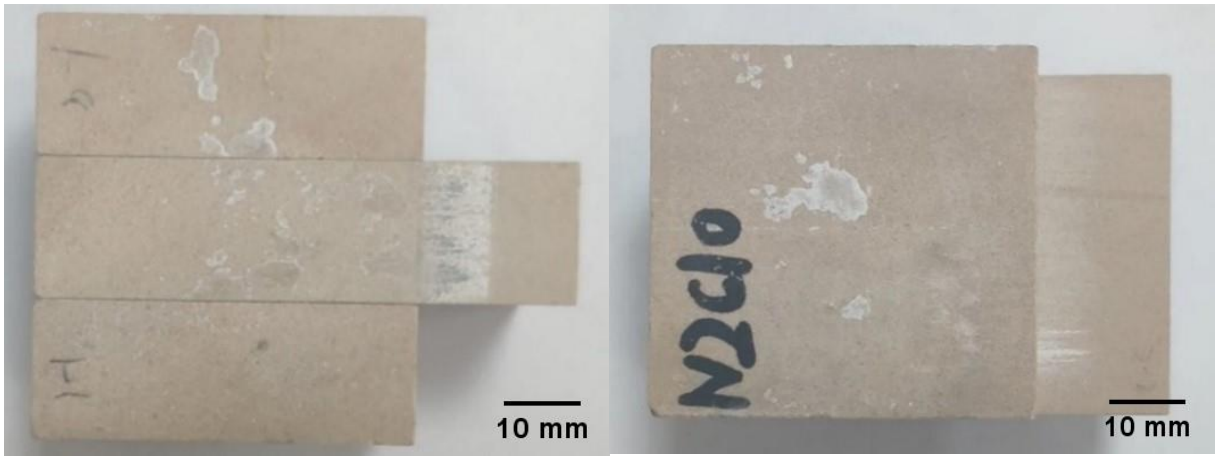

(a) (b)

Fig. 1. Sandstone fracture specimen for double-direct shear tests: (a) Plane view; and (b) Section view.

Fig. 2a and b presents images of the sandstone specimen used in the experiment under single- and cross-polarization, respectively. In Fig. 2a, brecciated quartz is evident, exhibiting poor sorting and rounding. Additionally, other minerals include black clayey debris, chloritized muscovite (mineral grains appear pale green), clay-shaped plagioclase with a rough surface, and argillaceous material between the grains. Fig. 2b shows quartz with an interference color of first-order white, plagioclase with an interference color of first-order grayish, and muscovite with its interference color concealed due to surrounding minerals. The sandstone exhibits a fine-grained, blocky structure. Particles are poorly sorted, and the filler between particles is heterogeneous (~20%). The background mass predominantly consists of clay minerals. The sandstone predominantly consists of quartz (~55%), plagioclase (~20%), and muscovite (~4%) in terms of their respective proportions. Additionally, there are trace amounts of clayey debris. The quartz is predominantly semi-automorphic and granular, with a particle size range of 0.1–0.32 mm. The plagioclase is mainly semi-automorphic and plate-like, with some instances of weathered plagioclase with a particle size range of 0.27–0.1 mm. The muscovite primarily takes the form of flakes, with some exhibiting chloritization and a particle size range of 0.05–0.1 mm.

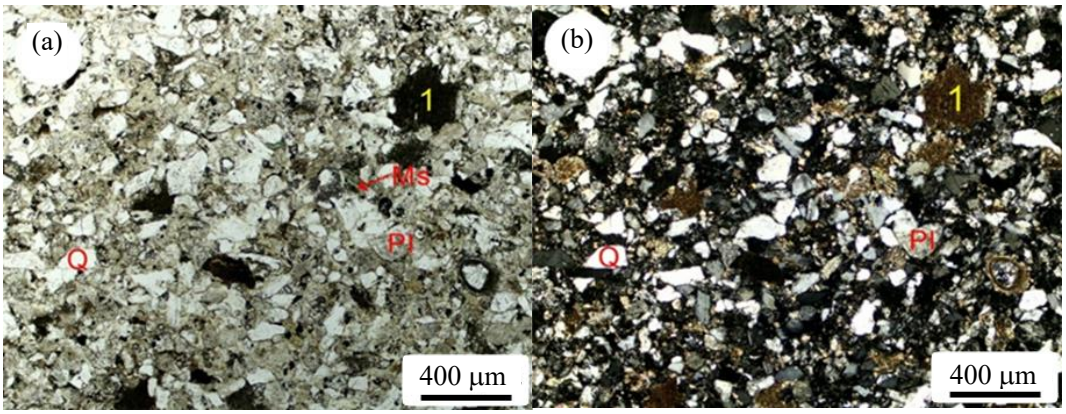

Fig. 2. Polarization images of the sandstone under the ZSY-2-1 T microscope: (a) Single polarization image (10×5); and (b) Orthogonal polarization image (10×5).

2.2. Experimental apparatus

The experimental setup utilized in this study is illustrated in Fig. 3a and consists of a rigid triaxial loading apparatus. This apparatus comprises separate axial, shear, and lateral loading systems, and is equipped with measurement systems for axial, tangential, and lateral loadings and displacements. The frame stiffness exceeds 0.7 GN/m, with the maximum loading capacities in the three directions being 300 kN, 200 kN, and 100 kN, respectively. The loading can be applied in either force or displacement modes. In the case of force-based loading, the loading rate ranges from 5 N/s to 5 kN/s, while for displacement-based loading, the displacement rate ranges from 0.01 mm/min to 50 mm/min. Fig. 3b illustrates the loading configuration. The platens and loading blocks employed in this loading device are fabricated using additive manufacturing techniques. In order to minimize friction between the specimen's surface and the loading block during the experiment, a copper sheet coated with Vaseline is placed in contact.

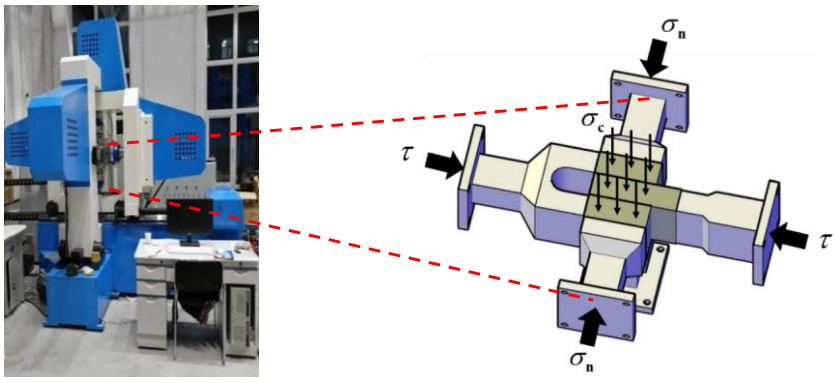

(a) (b)

Fig. 3. (a) True triaxial loading apparatus and (b) double-direct shear loading configuration. The red dotted line indicates the position of the platen (b) relative to the loading apparatus (a).

2.3. Experimental procedure

The range of applied normal and lateral stresses in this study was determined based on the conditions of the double-direct shear tests and the strength of the sandstone specimens (compressive strength <15 MPa). Three lateral stresses were selected: 0 MPa, 5 MPa, and 10 MPa, with four normal stress magnitudes chosen: 0.5 MPa, 2 MPa, 5 MPa, and 10 MPa. Shear velocities were set to 1 μm/s, 10 μm/s, and 100 μm/s, in accordance with velocity-stepping experiments. Stable sliding was observed within the range of 10–100 μm/s during the experiments conducted with normal stresses of 5 MPa and 10 MPa. Consequently, three additional shear velocities (60 μm/s, 70 μm/s, and 80 μm/s) were introduced for experiments with normal stresses of 0.5 MPa and 2 MPa. The 12 specimens were divided into 4 groups of experiments, with each group subjected to an identical normal stress while varying lateral stresses (0 MPa, 5 MPa, and 10 MPa, respectively), as detailed in Table 1.

Table 1
Experimental design.

Specimen No.	Normal stress (MPa)	Lateral stress (MPa)	Shear velocity (μm/s)
1	0.5	0	1→10→60→70→80→100→10
2	0.5	5	1→10→60→70→80→100→10
3	0.5	10	1→10→60→70→80→100→10
4	2	0	1→10→70→80→90→100→10
5	2	5	1→10→70→80→90→100→10
6	2	10	1→10→70→80→90→100→10
7	5	0	1→10→100→10
8	5	5	1→10→100→10
9	5	10	1→10→100→10
10	10	0	1→10→100→10
11	10	5	1→10→100→10
12	10	10	1→10→100→10

Fig. 4 illustrates the variation in stress with time during loading, using the example of a test at a normal stress of 10 MPa and a lateral stress of 5 MPa. The experimental procedure involves the following steps: (1) The normal and lateral stresses are loaded to 10 MPa and 5 MPa, respectively, at identical loading rates. After reaching the specified stress levels, they are maintained for 5 min. (2) Shear stress is applied in displacement-control mode, and the shear test is conducted at a constant shear velocity of 1 μm/s. (3) Velocity-stepping tests are performed with step velocities of 1–10 μm/s, 10–100 μm/s, and 100–10 μm/s. Throughout these tests, the shear displacements at each velocity step approximately range between 1 mm and 2 mm. The maximum shear displacement was ~20 mm.

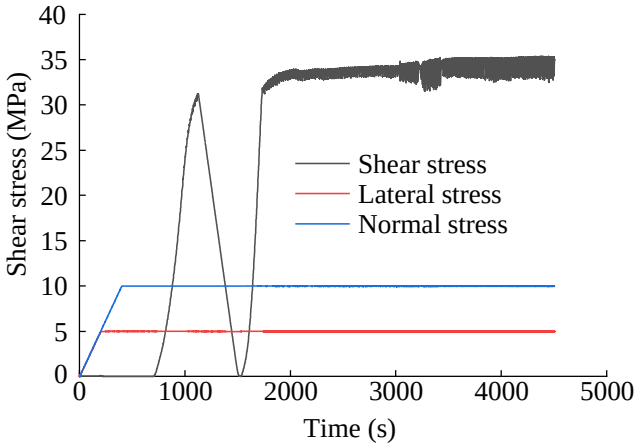

Fig. 4. Example illustrating the loading process.

The friction coefficient μ is calculated as

$$\mu=\frac{F_S}{2F_N}-\mu_f \qquad (1)$$

where F_N is the normal force, F_S is the shear force, and μ_f is the friction coefficient between the rig and the specimen after friction reduction. According to the test results, at a lateral stress of 5 MPa, the value of μ_f is determined to be 0.002, whereas at a lateral stress is 10 MPa, the value of μ_f is 0.00133.

In order to quantify the roughness of the sliding surfaces, an Artec Spider laser scanner (see Fig. 5) was employed to capture the 3D morphology of both the pre- and post-test sliding surfaces. This enables the calculation of their joint roughness coefficient (JRC) values (Jang et al., 2014). To optimize feature point capture, it is essential to maintain a low scanning speed while ensuring the structural integrity of the specimen surfaces during the scanning process.

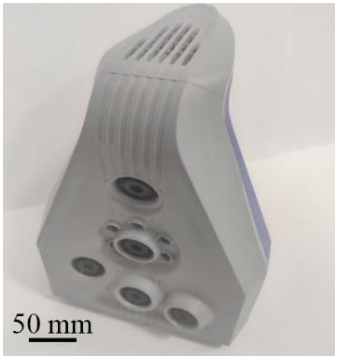

Fig. 5. Artec Spider laser scanner.

3. Results

3.1. Relationship between friction coefficient and shear displacement

Fig. 6 presents the friction coefficient-shear displacement curves for sandstone under different testing conditions, with a total shear displacement of ~10 mm for each test group. The specimen undergoes elastic deformation in the initial stage of the test, during which the friction coefficient increases linearly with shear displacement and eventually reaches its maximum value. Following an elastic run-in of ~0.5 mm, the applied shear force surpasses the frictional resistance, reactivating the sliding surfaces. Subsequently, as the shear displacement increases, the friction coefficient remains relatively constant while exhibiting stick-slip behavior.

By comparing the friction coefficient-shear displacement curves under different loading conditions, it is observed that a significant decrease in the friction coefficient occurs after reaching its peak in three specific loading conditions (i.e. σ_n = 2 MPa with σ_c = 10 MPa, σ_n = 0.5 MPa with σ_c = 5 MPa, and σ_n = 0.5 MPa with σ_c = 10 MPa), as depicted by the green curve in Fig. 6b and the green and black curves in Fig. 6c. The lateral stress is considerably greater than the normal stress (5–20 times) under these three stress conditions. Therefore, the substantial frictional resistance provided by the lateral stress leads to an increase in the peak shear stress. However, after the initiation of sliding, the influence of lateral stress diminishes, resulting in a subsequent decrease in post-peak shear stress towards residual strength. Consequently, the results of these three experimental sets will not be further analyzed in subsequent analyses.

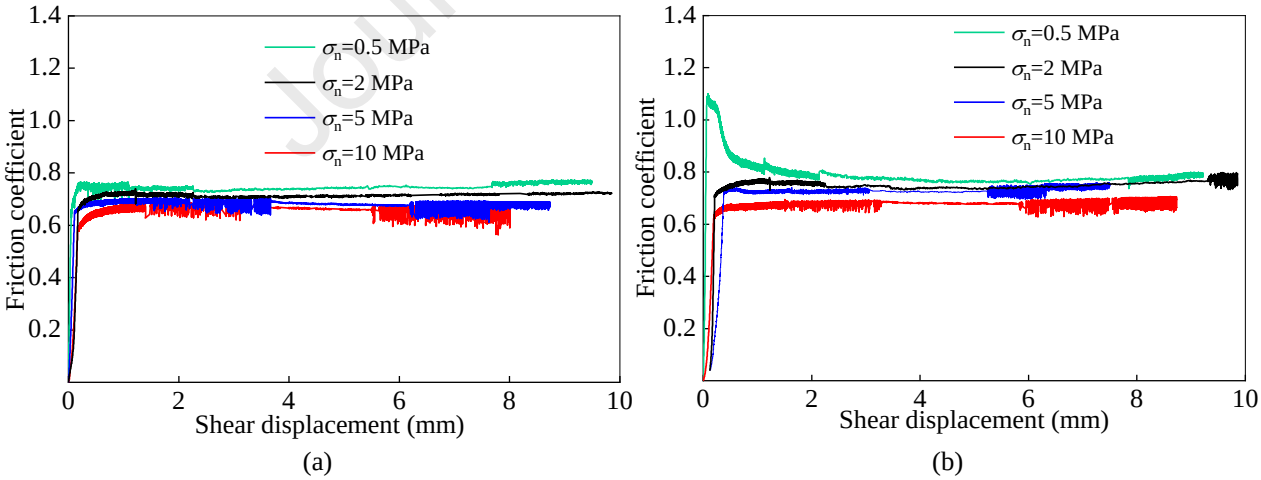

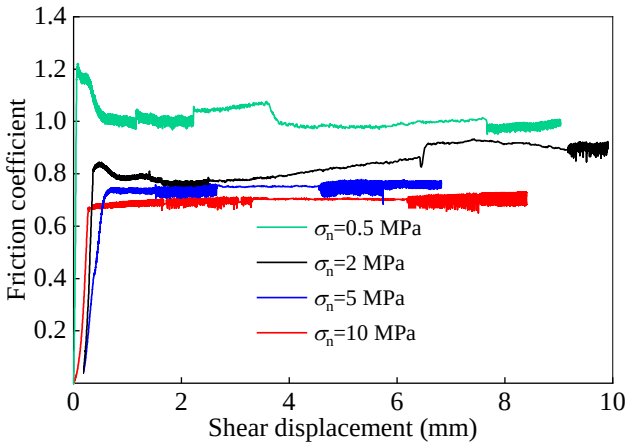

(c)

Fig. 6. Relationship between friction coefficient and shear displacement for lateral stresses of (a) 0, (b) 5 MPa, and (c) 10 MPa.

3.2. Effect of normal stress on friction coefficient

The relationship between the normal stress and the friction coefficient of the sandstone fracture at various shear rates is illustrated in Fig. 7a–c when the lateral stress is 0 MPa, 5 MPa, and 10 MPa, respectively. It can be observed that the friction coefficient decreases with increasing normal stress at each shear rate. However, it is crucial to note that the friction coefficient varies independently with different shear rates. Moreover, under varying stress conditions, the friction coefficient exhibits both an increasing and a decreasing response to changes in shear rate.

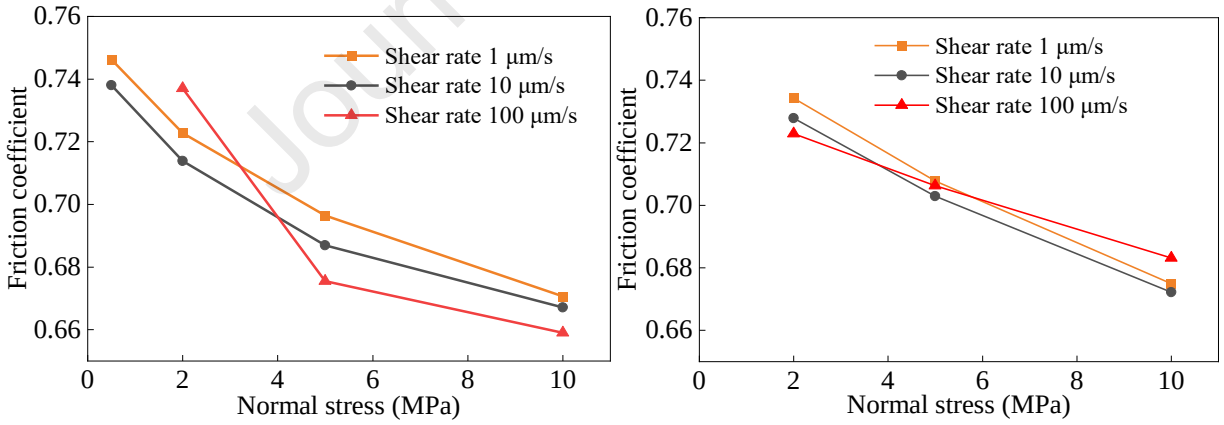

(a) (b)

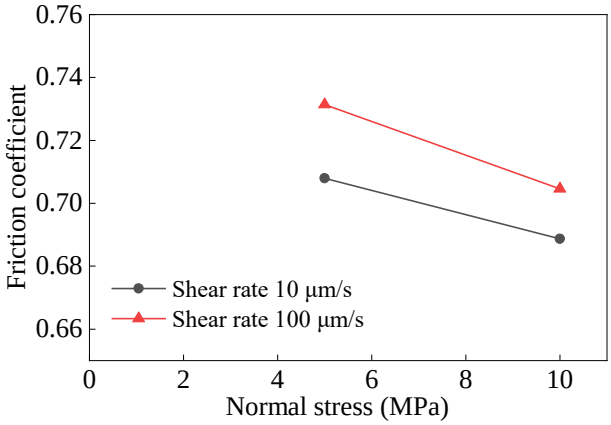

(c)

Fig. 7. Relationship between the friction coefficient and normal stress under lateral stresses of (a) 0 MPa, (b) 5 MPa, and (c) 10 MPa, with shear rates of 1 μm/s, 10 μm/s, and 100 μm/s.

After shear tests, the surfaces of the specimens depicted in Fig. 8 display varying degrees of frictional grooves, which become deeper and more numerous as the normal stress increases under the lateral stress of 0 MPa.

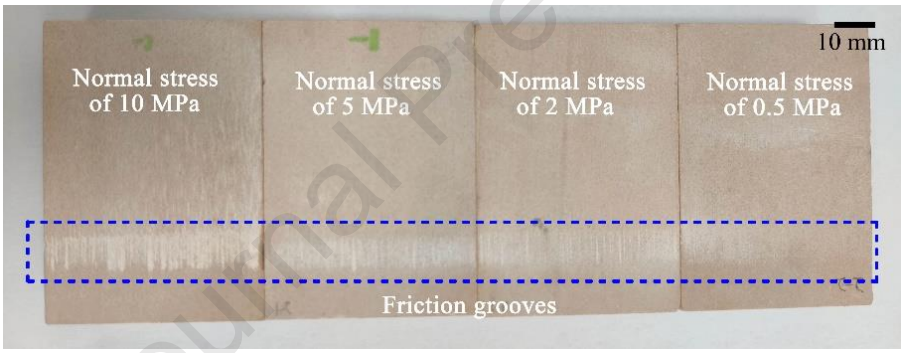

Fig. 8. Post-shear sandstone surfaces under different normal stresses when σ_c = 0 MPa. The blue dotted box marks the friction grooves.

The frictional groove section of the specimen was scanned with a maximum sampling accuracy of 0.05 mm, and its 3D morphology (Fig. 9) was obtained after calibration and noise removal techniques were applied. A MATLAB program was utilized to calculate the surface roughness of the specimen (Jang et al., 2014). Table 2 presents the JRC values for sandstone surfaces before and after shearing. The results presented in Table 2 demonstrate an observed increase in the JRC value of sandstone surfaces after the shear test, indicating that the test leads to a rougher surface. This is consistent with macroscopic observations during testing. The post-shear JRC value increases with normal stress, and decreases with lateral stress, implying that wear on the sandstone surfaces becomes more severe under higher normal stress while being mitigated under higher lateral stress.

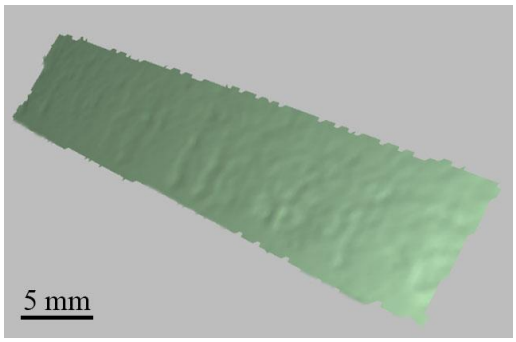

Fig. 9. 3D morphology of the frictional groove section of the specimen.

Table 2

Pre- and post-shear JRC values of sandstone surfaces under different testing conditions.

Normal stress (MPa)	Lateral stress (MPa)	Pre-shear JRC	Post-shear JRC
0.5	0	1.1548	1.6703
2	0	1.1548	2.9988
2	5	1.1548	2.5217
5	0	1.1548	6.1132
5	5	1.1548	5.6994
5	10	1.1548	5.0983
10	0	1.1548	8.4483
10	5	1.1548	7.8976
10	10	1.1548	7.4372

3.3. Effect of lateral stress on the friction coefficient

The relationship between the friction coefficient and the lateral stress of the sandstone fracture at different shear rates is depicted in Fig. 10a, b, and c for normal stresses of 2 MPa, 5 MPa, and 10 MPa, respectively. The friction coefficient increases with the increase in lateral stress across all shear rates. Different shear rates correspond to different friction coefficients. Similar to Fig. 7, the friction coefficient does not exhibit a monotonic correlation with shear rates, thus it is important to further investigate this effect.

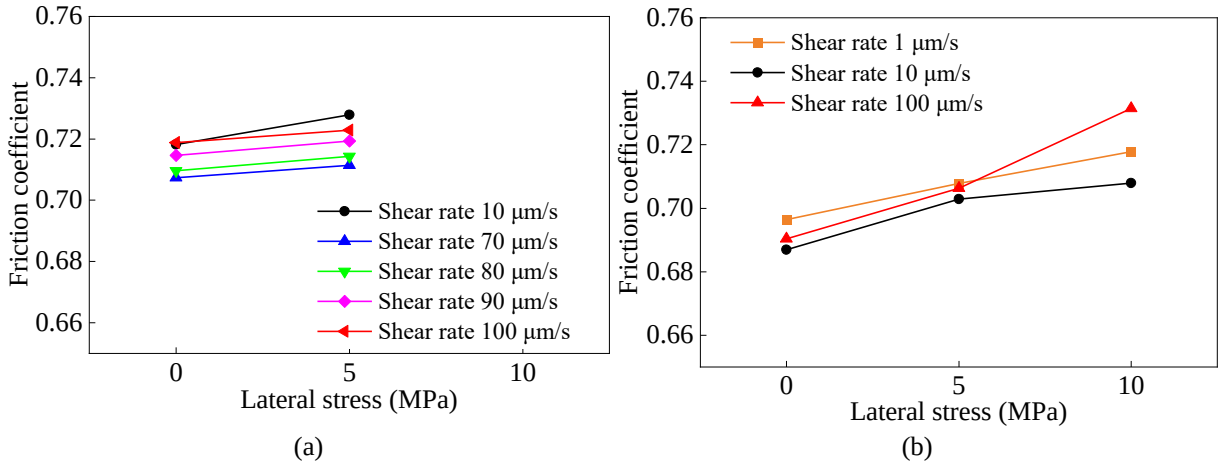

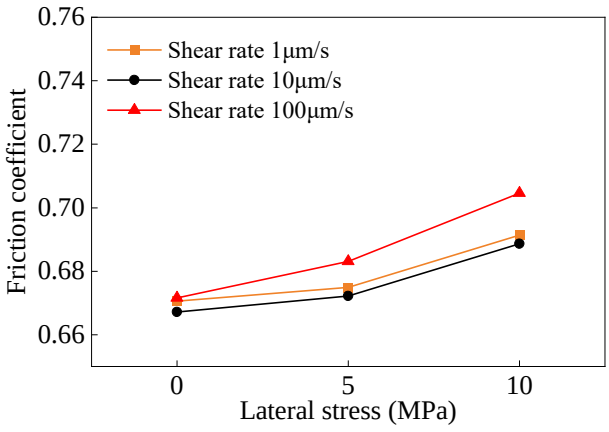

(c)

Fig. 10. Relationship between the friction coefficient and lateral stress under normal stresses of (a) 2 MPa, (b) 5 MPa, and (c) 10 MPa, with shear rates of 1 μm/s, 10 μm/s, and 100 μm/s.

The post-test surfaces of three specimens are depicted in Fig. 11, under the normal stress of 5 MPa and varying lateral stresses. Table 2 presents the JRC values obtained from the scanned surfaces. The impact of lateral stress on the surfaces pre- and post-shearing reveals a reduction in JRC as the lateral stress increases.

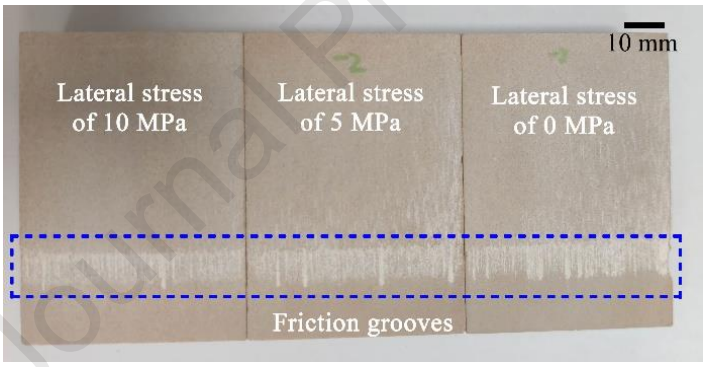

Fig. 11. Post-shear sandstone surfaces under different lateral stresses when σ_n = 5 MPa. The blue dotted box marks the friction grooves.

3.4. Effect of lateral stress on the rate dependence of friction coefficient

Fig. 12a–d illustrates the relationship between the friction coefficient and shear rate of sandstone fractures under varying normal stresses (0.5 MPa, 2 MPa, 5 MPa, and 10 MPa) in the absence of lateral stress. When the normal stresses are 0.5 MPa and 2 MPa, the friction coefficient exhibits a continuous decrease as the shear velocity is changed from 1 μm/s to 10 μm/s, then to 60 μm/s, and further to 70 μm/s, indicating velocity-weakening behavior. However, an increase in the friction coefficient is observed when the shear velocity increases from 70 μm/s to 80 μm/s and then to 100 μm/s, indicating velocity-strengthening behavior. Initially, velocity-weakening behavior is observed when the normal stress is 5 MPa and 10 MPa, followed by a transition to velocity-strengthening as the shear rate increases.

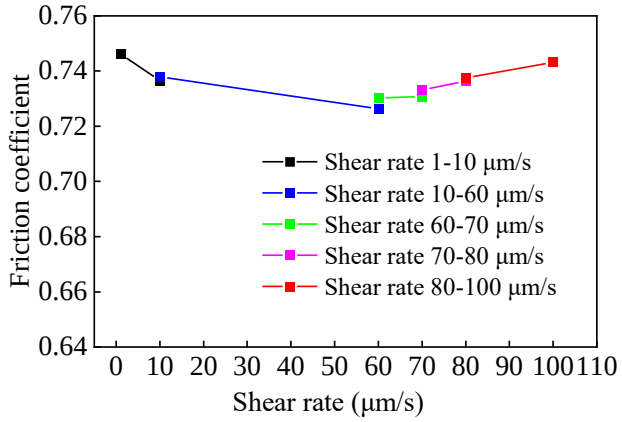

(a)

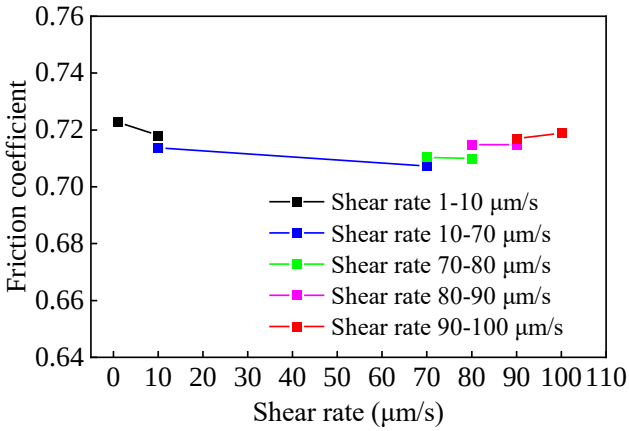

(b)

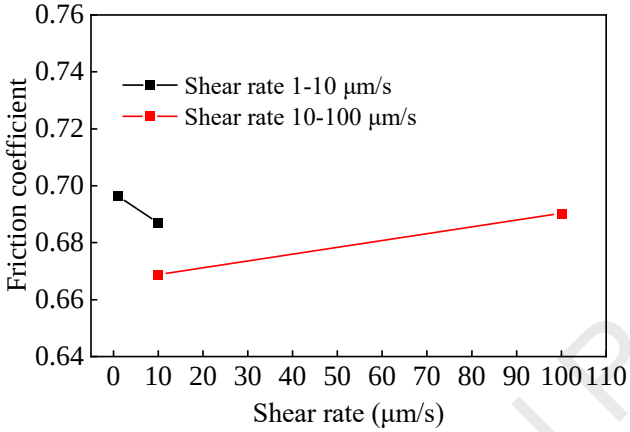

(c)

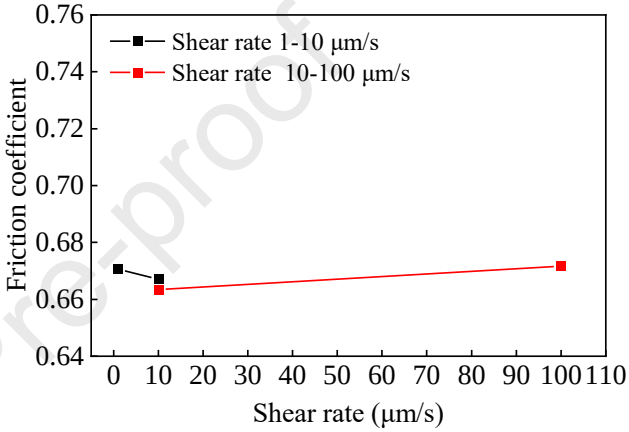

(d)

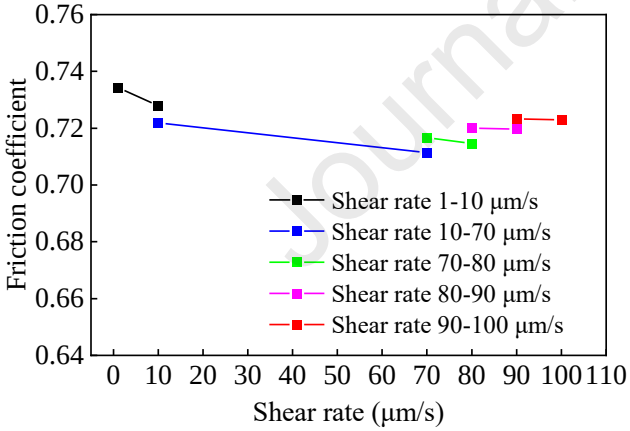

(e)

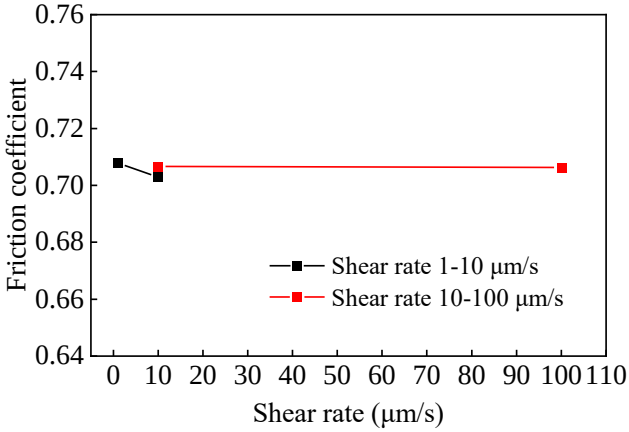

(f)

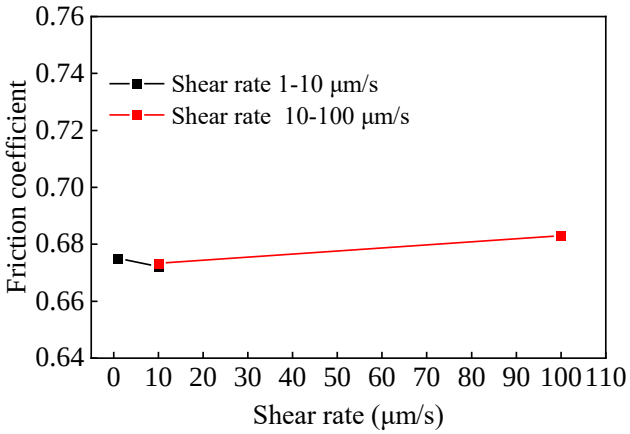

(g)

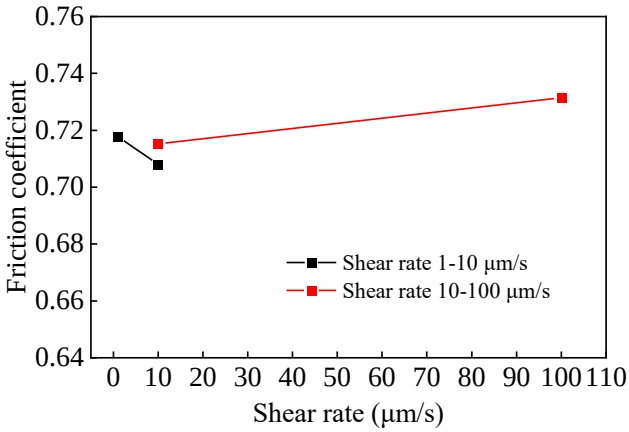

(h)

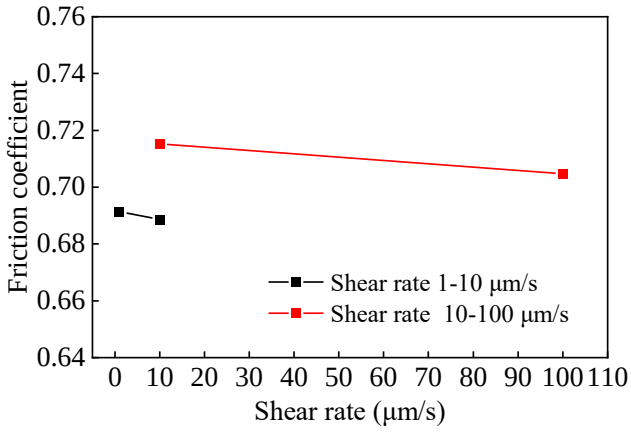

(i)

Fig. 12. Relationship between the friction coefficient and shear rate under different lateral and normal stresses: (a) σ_n = 0.5 MPa, and σ_c = 0 MPa; (b) σ_n = 2 MPa, and σ_c = 0 MPa; (c) σ_n = 5 MPa, and σ_c = 0 MPa; (d) σ_n = 10 MPa, and σ_c = 0 MPa; (e) σ_n = 2 MPa, and σ_c = 5 MPa; (f) σ_n = 5 MPa, and σ_c = 5 MPa; (g) σ_n = 10 MPa, and σ_c = 5 MPa; (h) σ_n = 5 MPa, and σ_c = 10 MPa; and (i) σ_n = 10 MPa, and σ_c = 10 MPa.

The relationship between the friction coefficient and shear rate under a lateral stress of 5 MPa is depicted in Fig. 12e–g, with normal stresses of 2 MPa, 5 MPa, and 10 MPa, respectively. When the normal stress is 2 MPa, the friction coefficient decreases at each shear velocity step, indicating the velocity-weakening behavior. However, this velocity-weakening phenomenon gradually diminishes as the shear velocity increases. At the normal stress of 5 MPa, velocity-weakening is observed as the shear velocity steps from 1 μm/s to 10 μm/s, while the friction coefficient undergoes minimal change as the shear velocity steps from 10 μm/s to 100 μm/s. Under the normal stress of 10 MPa, velocity-weakening transitions to velocity-strengthening as the shear rate increases.

The relationship between the friction coefficient and shear rate of the sandstone fracture under the lateral stress of 10 MPa, at normal stresses of 5 MPa and 10 MPa, is depicted in Fig. 12h and i, respectively. When the normal stress is 10 MPa, all shear velocity steps represent velocity-weakening. At the normal stress of 5 MPa, the friction coefficient weakens as the shear velocity increases from 1 μm/s to 10 μm/s, while it exhibits a velocity-strengthening trend as the velocity increases from 10 μm/s to 100 μm/s.

In summary, when the lateral stress is significantly smaller than the normal stress (as shown in Fig. 12a–d and g), shear velocity steps at low velocities (<70 μm/s) indicate a velocity-weakening response, while velocity steps at high velocities (≥70 μm/s) demonstrate a propensity for velocity-strengthening. When the lateral stress is equal to or greater than the normal stress (as shown in Fig. 12e, f, and i), the velocity-weakening phenomenon persists at low shear velocities, but the velocity-strengthening response disappears at high shear velocities. However, an anomaly is apparent when the normal stress is 5 MPa and the lateral

stress is 10 MPa (as depicted in Fig. 12h). This could be attributed to the excessively large span of the velocity step under this specific condition.

3.5. Effect of shear displacement on the friction coefficient

When analyzing the influence of shear displacement on the friction coefficient, it is important to note that the shear test achieves stable sliding after ~1 mm of initial shear displacement. This initial shear offset corresponds to a shear rate of 1 μm/s. Consequently, the analysis disregards the friction coefficient at a shear rate of 1 μm/s and commences solely from a shear velocity of 10 μm/s. Concerning the impact of shear displacement, the phenomenon that the friction coefficient decreases with increasing shear displacement is referred to as displacement-weakening, whereas an increase in the friction coefficient with shear displacement is termed displacement-strengthening.

The relationship between the shear displacement and friction coefficient of the sandstone fracture under normal stress of 2 MPa and lateral stresses of 0 MPa and 5 MPa is depicted in Fig. 13a and b, respectively. At a shear velocity of 10 μm/s, an increase in shear displacement results in a decrease in the friction coefficient. Conversely, at shear velocities of 70 μm/s, 80 μm/s, 90 μm/s, and 100 μm/s, the friction coefficient increases as the shear displacement increases.

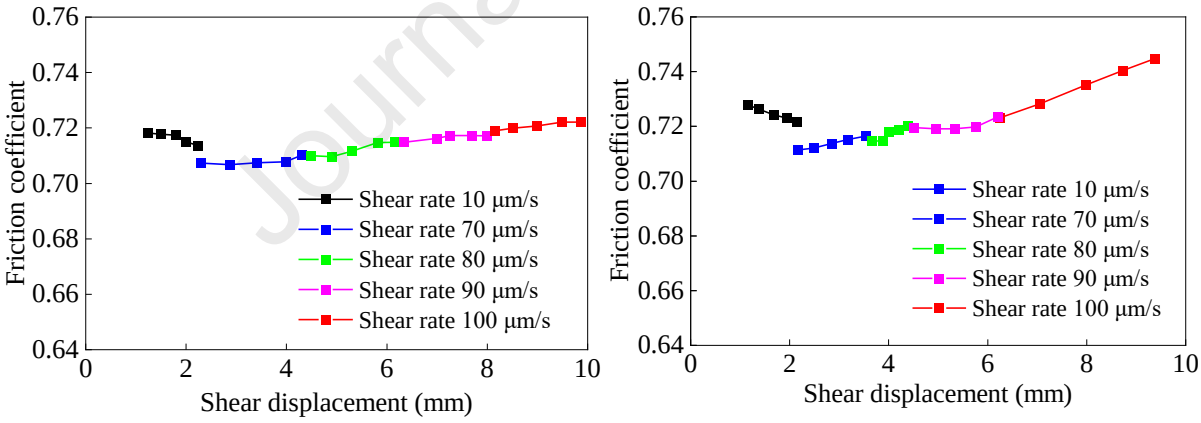

Fig. 13. Relationship between the friction coefficient and shear displacement under different shear rates and lateral stresses when σ_n = 2 MPa: (a) σ_c = 0 MPa; and (b) σ_c = 5 MPa.

4. Modified rate-state friction model

Rate-state friction (RSF) constitutive models are based on extensive shear experiments and are widely accepted. The RSF model comprises two equations: the main equation of rate and state friction and a state evolution equation governing the response of state variables to changes in loading velocity. While Dieterich (1979) and Ruina (1983) utilized the same main

equation (Eq. (2)), they employed different state evolution equations, as depicted in Eqs. (3) and (4):

$$\mu = \mu_0 + a\ln\left(\frac{V}{V_0}\right) + b\ln\left(\frac{V_0\theta}{D_c}\right) \quad \text{(RSF equation)} \qquad (2)$$

$$\frac{\mathrm{d}\theta}{\mathrm{d}t} = 1 - \frac{V\theta}{D_c} \quad \text{(Aging form of the state evolution equation)} \qquad (3)$$

$$\frac{\mathrm{d}\theta}{\mathrm{d}t} = -\frac{V\theta}{D_c}\ln\left(\frac{V\theta}{D_c}\right) \quad \text{(Slip form of the state evolution equation)} \qquad (4)$$

where V_0 is a reference sliding velocity; V is the updated sliding velocity; μ_0 is the initial friction coefficient when the sliding velocity is V_0; and a and b are the material-specific constants describing whether the material exhibits velocity-strengthening or velocity-weakening response. with a representing the immediate rise in friction as the sliding velocity increases, and b representing the magnitude of the displacement-dependent transition to a new state; θ is the state variable; and D_c is the critical slip distance.

The parameters a and b in the rate-state friction constitutive model were determined using our experimental observations, as provided in Tables 3 and 4. The relationship between the initial friction coefficient μ_0 and normal and lateral stresses at different shear rates is illustrated in Fig. 14. It can be observed that the initial friction coefficient decreases with an increase in normal stress, but increases with an increase in lateral stress.

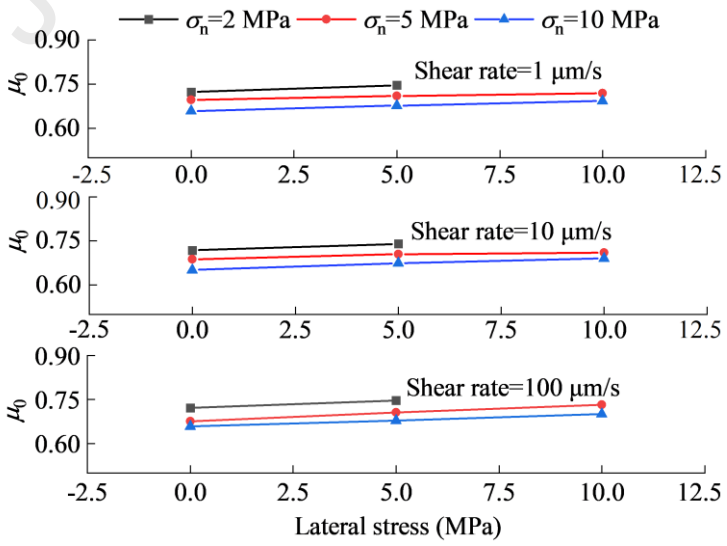

Fig. 14. Relationship between the initial friction coefficient and normal and lateral stresses.

Table 3

Values of parameters *a* and *b* under different testing conditions.

Normal stress (MPa)	Lateral stress (MPa)	Shear velocity step (μm/s)	*a*	*b*
0.5	0	1→10	0.0112	0.016
0.5	0	10→60	0.0205	0.0217
0.5	0	60→70	0.054	0.045
0.5	0	70→80	0.0758	0.0446
0.5	0	80→100	0.0567	0.05
2	0	1→10	0.0089	0.0115
2	0	10→70	0.0201	0.0233
2	0	70→80	0.0173	0.0143
2	0	80→90	0.0447	0.0301
2	0	90→100	0.0297	0.0129
2	5	1→10	0.01	0.013
2	5	10→70	0.0075	0.0135
2	5	70→80	0.0646	0.0624
2	5	80→90	0.0306	0.0068
2	5	90→100	0.0229	0.0192
5	0	1→10	0.005	0.0091
5	0	10→100	0.017	0.008
5	5	1→10	0.0173	0.0195
5	5	10→100	0.0053	0.0056
5	10	1→10	0.0266	0.0312
5	10	10→100	0.014	0.0055
10	0	1→10	0.0123	0.017
10	0	10→100	0.0078	0.0064
10	5	1→10	0.0213	0.0244
10	5	10→100	0.0084	-0.0053
10	10	1→10	0.023	0.0271
10	10	10→100	0.0024	-0.009

Table 4

Values of initial friction coefficient under different testing conditions.

Normal stress (MPa)	Lateral stress (MPa)	Shear velocity (μm/s)	μ_0
0.5	0	1	0.74617
0.5	0	10	0.73793
0.5	0	60	0.73938
2	0	1	0.7228
2	0	10	0.71814
2	0	70	0.70734
2	0	80	0.70966
2	0	90	0.7146
2	0	100	0.71884
2	5	1	0.73428
2	5	10	0.7279
2	5	70	0.71142
2	5	80	0.71437
2	5	90	0.71936
2	5	100	0.7229
5	0	1	0.6964
5	0	10	0.68691
5	0	100	0.69032
5	5	1	0.70779
5	5	10	0.70289
5	5	100	0.70631
5	10	1	0.71783
5	10	10	0.70794

5	10	100	0.73139
10	0	1	0.67064
10	0	10	0.66712
10	0	100	0.659
10	5	1	0.67497
10	5	10	0.67217
10	5	100	0.68311
10	10	1	0.69141
10	10	10	0.6887
10	10	100	0.70462

Fig. 15 illustrates the relationship between parameters *a* and *b* and lateral stress under different normal stresses. However, there is no significant correlation between coefficients *a* and *b* and lateral stresses. Therefore, we hypothesize that the primary influence of normal and lateral stresses is exerted upon the initial friction coefficient μ_0.

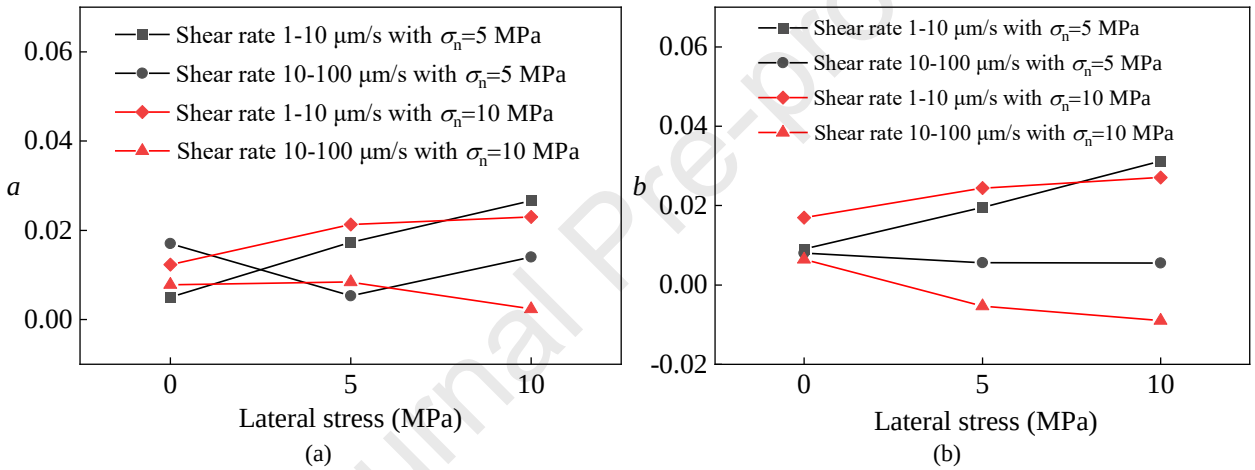

Fig. 15. Relationship of parameter *a* vs. lateral stress and *b* vs. lateral stress for the fracture under different testing conditions.

The initial friction coefficient μ_0 decreases with an increase in normal stress and increases with an increase in lateral stress. The initial friction coefficient is linearly correlated with the normal and lateral stresses, which can be described as follows:

$$\mu_0 = \mu_{0i} + A\sigma_n^{\phi} + B\sigma_c^{\phi} \qquad (5)$$

where μ_{0i} is a basic friction coefficient; *A* and *B* are the pre-factors conditioning the normal and lateral stresses, respectively; and $\sigma_n^{\phi} = \sigma_n / q_u$ and $\sigma_c^{\phi} = \sigma_c / q_u$ are the dimensionless normal and lateral stresses, respectively, in which q_u is the uniaxial compressive strength (UCS). For the sandstone used in this study, the UCS is 55 MPa.

A modified RSF model is obtained by combining the slip form of the state evolution equation with this redefined initial friction coefficient μ_0 in the main equation. The expression for the modified RSF model is therefore as follows:

$$\mu = \mu_{0i} + A\sigma_n' + B\sigma_c' + a\ln\left(\frac{V}{V_0}\right) + b\ln\left(\frac{V_0\theta}{D_c}\right) \qquad (6)$$

$$\frac{d\theta}{dt} = -\frac{V\theta}{D_c}\ln\left(\frac{V\theta}{D_c}\right)$$

Fig. 16a and b compares model predictions and experimental data for normal stresses of 5 and 10 MPa, regarding the relationship between the initial friction coefficient and lateral stress. Specifically, the basic friction coefficient (μ_{0i}) is 0.72433, the factor A is -0.33473, and the factor B is 0.1249. The friction coefficient correlates negatively with the normal stress, and positively with the lateral stress. Notably, the influence of normal stress on the friction coefficient is more than double that of lateral stress. Fig. 16 also compares the original RSF constitutive model and the modified version. The black line represents the fitting result of the original model, and the red line represents the fitting result of the modified model (Eq. (5)), which incorporates the influence of lateral stress and yields a superior fit for the initial friction coefficient.

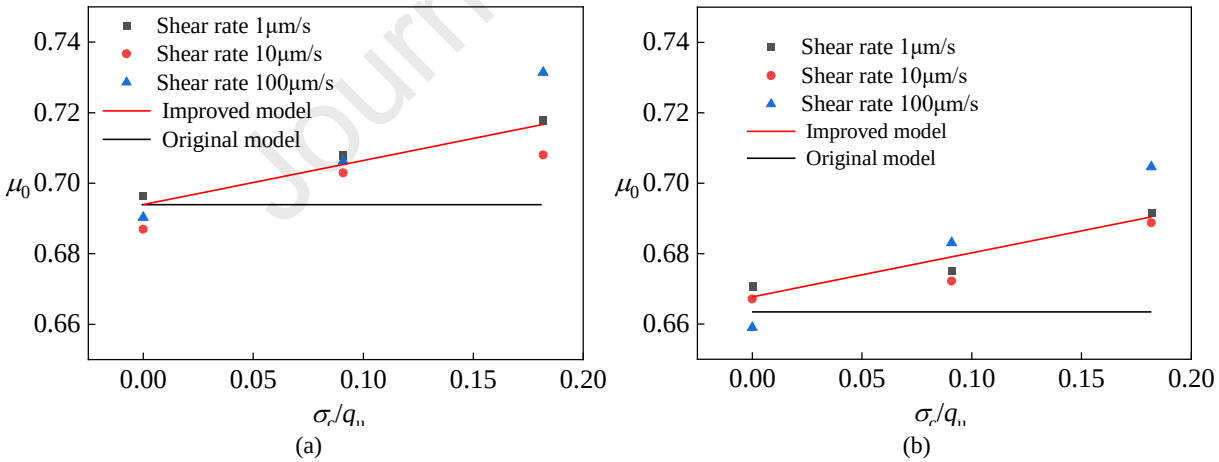

Fig. 16. Fitting results between the initial friction coefficient and lateral stress: (a) σ_n = 5 MPa; and (b) σ_n = 10 MPa.

5. Mechanisms of influence of lateral and normal stresses on friction

The present study postulates that the destruction of asperities on the fracture surface during frictional sliding leads to the generation of wear products, which serve as a primary factor that influences the variation in friction coefficient. These wear products transform sliding friction

into rolling friction on the fracture surface, resulting in a higher volume of wear products that return a reduced friction coefficient.

Firstly, we investigate the impact of lateral stress on the generation of wear products. When the normal stress remains constant, the Mogi–Coulomb strength criterion (Eq. (7)) indicates that lateral stress will enhance the shear strength of the rock (Al-Ajmi and Zimmerman, 2005). Consequently, this inherent increase in strength may reduce the failure of asperities on the surface, thereby reducing the amount of wear products. The results presented in Table 2 demonstrate that, under constant normal stress, the post-shear JRC value decreases as the lateral stress increases, which provides evidence for the mitigation of wear.

$$\tau_{oct} = \frac{1}{3}\sqrt{(\sigma_1 - \sigma_2)^2 + (\sigma_2 - \sigma_3)^2 + (\sigma_3 - \sigma_1)^2} \qquad (7)$$

Subsequently, we examine the influence of normal stress on the production of wear products. At low normal stress levels, dilation leads to fewer asperities being ruptured and a smaller quantity of wear products generated, resulting in a higher friction coefficient. However, at high normal stress levels, the increased constraint in the normal direction suppresses dilation, resulting in more pronounced failure of asperities and a larger volume of wear products. As the amount of wear products increases, the friction coefficient decreases due to rolling friction on fractures. It can be observed from Table 2 that the post-shear JRC value increases with an increase in normal stress, thus confirming the above speculation.

6. Conclusions

A true triaxial loading device was employed to conduct double-direct shear experiments on sandstone fractures. The objective was to investigate the frictional properties of rock fractures under different normal and lateral stresses.

The test data demonstrate that the friction coefficient of sandstone fractures increases with increasing lateral stress and decreases with increasing normal stress. For low shear velocities (in this study, <70 μm/s), the friction coefficient exhibits velocity-weakening behavior. For greater shear velocities (≥70 μm/s) and under small lateral stresses, the friction coefficient demonstrates a velocity-strengthening phenomenon, which diminishes with increasing lateral stress.

The utilization of the RSF model for the analysis of test data reveals that the initial friction coefficient decreases with increasing normal stress and increases with increasing lateral stress.

However, coefficients *a* and *b* show no significant correlation with either lateral stress or normal stress. Consequently, the initial friction coefficient was formulated as a function of both lateral and normal stresses, effectively incorporating the influence of both lateral stress and normal stress, through the derivation of a modified RSF model.

Finally, we propose mechanisms through which lateral and normal stresses affect the frictional properties of sandstone fractures. It is proposed that the application of lateral stress increases stress confinement and local strength of the asperities on the fracture surface, thereby leading to an increase in the friction coefficient of these sandstone fractures. Moreover, higher normal stress results in an elevated production of wear products on the fracture surfaces. Notably, the rolling friction coefficient of mineral particles is smaller than the sliding friction coefficient, resulting in a reduced friction coefficient on the sandstone fracture.

The underground gas storage is primarily constructed within sandstone formations, and thus this study exclusively focuses on investigating the frictional properties of fractures within sandstone. Although the research idea presented in this paper holds universal applicability, caution should be exercised when extrapolating the findings to other rock types. To address this limitation, future endeavors could encompass a broader range of rock types for experimental investigation.

Declaration of Competing Interest

The authors declare that they have no known competing financial interests or personal relationships that could have appeared to influence the work reported in this paper.

Acknowledgments

The research was supported by National Nature Science Foundation of China (Grant No. 42177157), the Science and Technology Program of Liaoning Province (Grant No. 2023JH1/10400003), and the Applied Basic Research Program of Liaoning Province (Grant No. 2023JH2/101300153). Xiaojun Yu is gratefully acknowledged for his contribution to this paper on the guidance of the triaxial loading device. DE gratefully acknowledges support from the G. Albert Shoemaker endowment.

References

Al-Ajmi, A.M., Zimmerman, R.W., 2005. Relation between the Mogi and the Coulomb failure criteria. Int. J. Rock. Mech. Min. Sci. 42 (3), 431–439.

Ben-David, O., Cohen, G., Fineberg, J., 2010. The dynamics of the onset of frictional slip. Science 330 (6001), 211–214.

Blanpied, M., Tullis, T., Weeks, J., 1987. Frictional behavior of granite at low and high sliding velocities. Geophys. Res. Lett. 14 (5), 554–557.

Brace, W.F., Byerlee, J.D., 1966. Stick-slip as a mechanism for earthquakes. Science 153 (3739), 990–992.

Collettini, C., Di Stefano, G., Carpenter, B., et al., 2014. A novel and versatile apparatus for brittle rock deformation. Int. J. Rock. Mech. Min. Sci. 66 (1), 114–123.

Cui, Y., Ma, S., Liu, L., 2005. Effect of lateral stress perturbation on frictional behavior: An experimental study. Seismol. Geol. 27 (4), 645–652.

Dieterich, J.H., 1979. Modeling of rock friction: 1. Experimental results and constitutive equations. J. Geophys. Res. 84 (B5), 2161–2168.

Dong, P., Xia, K., Guo, Y., 2018. Experimental study on stick-slip and dynamic rupture propagation of straight faults. Chin. J. Rock Mech. Eng. 37 (Supp. 2), 3990–3997 (in Chinese).

Ellsworth, W.L., 2013. Injection-induced earthquakes. Science 341 (6142), 1225942.

Feng, X.T., Wang, G., Zhang, X., et al., 2021. Experimental method for direct shear tests of hard rock under both normal stress and lateral stress. Int. J. Geomech. 21 (3), 04021013.

Han, W., Kang, T., 2013. Experimental study of influence of asperity on static friction coefficient for polished rock surface. Rock Soil Mech. 34 (3), 674–678 (in Chinese).

He, M., Li, Q., Li, X., Xu, L., Kühn, M., 2021. Hydromechanical behaviors of andesite under different stress states during fluid injection. J. Rock Mech. Geotech. Eng. 13 (4), 727–744.

Jang, H.S., Kang, S.S., Jang, B.A., 2014. Determination of joint roughness coefficients using roughness parameters. Rock Mech. Rock Eng. 47 (6), 2061–2073.

Kilgore, B.D., Blanpied, M.L., Dieterich, J.H., 1993. Velocity dependent friction of granite over a wide range of conditions. Geophys. Res. Lett. 20 (10), 903–906.

Leeman, J.R., Marone, C., Saffer, D.M., 2018. Frictional mechanics of slow earthquakes. J. Geophys. Res. – Solid Earth 123 (9), 7931–7949.

Leeman, J.R., Saffer, D.M., Scuderi, M.M., Marone, C., 2016. Laboratory observations of slow earthquakes and the spectrum of tectonic fault slip modes. Nat. Commun. 7 (1), 11104.

Li, D., Yang, B., Jin, J., Liu, D., She, J., Zhang, D., 2023. Friction coefficients calculation via surface roughness characterization for tight sedimentary rocks. Arab. J. Sci. Eng. 48 (7), 9287–9298.

Li, J., Liu, X., Hao, J., Cai, D., Fang, Y., Geng, N., 1987. The *b* value of acoustic emission in frictional sliding of rocks. Northwest. Seismol. J. 9 (4), 34–38 (in Chinese).

Liu, Y., He, C., 2023. Friction of hornblende and tremolite at hydrothermal conditions with low effective normal stress and high pore pressure. Tectonophysics 863 (1), 230002.

Marone, C., 1998. The effect of loading rate on static friction and the rate of fault healing during the earthquake cycle. Nature 101 (6662), 1143–1152.

Marone, C., Raleigh, C.B., Scholz, C.H., 1990. Frictional behavior and constitutive modeling of simulated fault gouge. J. Geophys. Res. – Solid Earth 95 (B5), 7007–7025.

Mehrishal, S., Sharifzadeh, M., Shahriar, K., Song, J.J., 2016. An experimental study on normal stress and shear rate dependency of basic friction coefficient in dry and wet limestone joints. Rock Mech. Rock Eng. 49 (12), 4607–4629.

Miao, A., Ma, S., Hou, L., Yao, L., 2012. Velocity-dependence transition of friction for halite gouge and its significance implication in seismology. Chin. J. Geophys. 55 (10), 3307–3317 (in Chinese).

Noda, H., 2023. Thermoelastic instability on a frictional surface and its implication for size effect in friction experiments. Earth Planets Space 75 (1), 71–83.

Ruina, A., 1983. Slip instability and state variable friction laws. J. Geophys. Res.– Solid Earth 88 (B12), 10359–10370.

Tatnell, L., Dyson, A.P., Tolooiyan, A., 2021. Coupled Eulerian-Lagrangian simulation of a modified direct shear apparatus for the measurement of residual shear strengths. J. Rock Mech. Geotech. Eng. 13 (5), 1113–1123.

Wang, F., Feng, X.-T., Zhou, Y., Yu, X., 2023b. Experimental study on failure evolution mechanism of clastic rock considering cementation and intermediate principal stress. J. Rock Mech. Geotech. Eng. 15 (7), 1636–1650.

Wang, P., Yang, T., Wang, S., Liu, H., Zhang, Z., 2023a. Study on the slip characteristics of rock inhomogeneous friction interface. Geomech. Geophys. Geo-Energ. Geo-Resour. 9 (1), 40–57.

Zhang, C., Xu, J., Jin, S., Cui, G., Guo, Y., Li, L., 2023. Sliding modes of fault activation under constant normal stiffness conditions. J. Rock Mech. Geotech. Eng. 15 (5), 1213–1225.

Zhong, Z., Xu, C., Hu, Y., Zhang, F., Wu, F., Li, B., 2024. Frictional strength and sliding behaviors of an analogue rock-fault structure: A laboratory study. Int. J. Rock. Mech. Min. Sci. 174 (1), 105665–105685.

Zhong, Z., Xu, C., Wang, L., Hu, Y., Zhang, F., 2023. Experimental investigation on frictional properties of stressed basalt fractures. J. Rock Mech. Geotech. Eng. 15 (6), 1457–1475.

Zhechao Wang obtained his MSc degree from the Institute of Rock and Soil Mechanics, Chinese Academy of Sciences in 2006, and his PhD degree from the University of Calgary, Canada in 2010. He is currently a professor at Northeastern University, where he teaches and conducts research in rock and soil mechanics. His research primarily focuses on the fundamental theories and key technologies in the field of underground storage engineering.

Declaration of interests

☒ The authors declare that they have no known competing financial interests or personal relationships that could have appeared to influence the work reported in this paper.

☐The authors declare the following financial interests/personal relationships which may be considered as potential competing interests: